How does the space-borne radar blind-zone affect derived surface snowfall statistics in polar regions?

Maximilian Maahn,[1] Clara Burgard,[1] Susanne Crewell,[1] Irina V. Gorodetskaya,[2] Stefan Kneifel,[3] Stef Lhermitte,[2] Kristof Van Tricht,[2] Nicole P. M. van Lipzig[2]

Corresponding author: M. Maahn, Institute for Geophysics and Meteorology, University of Cologne, Germany. (mmaahn@meteo.uni-koeln.de)

[1]Institute for Geophysics and Meteorology, University of Cologne, Germany.

[2]Department of Earth & Environmental Sciences, KU Leuven, Belgium.

[3]Department of Atmospheric and Oceanic Sciences, McGill University, Canada.

This article has been accepted for publication and undergone full peer review but has not been through the copyediting, typesetting, pagination and proofreading process, which may lead to differences between this version and the Version of Record. Please cite this article as doi: 10.1002/2014JD022079

Abstract. Global statistics of snowfall are currently only available from the CloudSat satellite. But CloudSat cannot provide observations of clouds and precipitation within the so-called blind-zone, which is caused by ground-clutter contamination of the CloudSat radar and covers the last 1200 m above land/ice surface. In this study, the impact of the blind-zone of CloudSat on derived snowfall statistics in polar regions is investigated by analyzing three 12-month datasets recorded by ground-based Micro Rain Radars (MRR) at the Belgian Princess Elisabeth station in East Antarctica and at Ny-Ålesund and Longyearbyen in Svalbard, Norway. MRR radar reflectivity profiles are investigated in respect to vertical variability in the frequency distribution, changes in the number of observed snow events and impacts on total precipitation. Results show that the blind-zone leads to reflectivity being underestimated by up to 1 dB, the number of events being altered by ±5% and the precipitation amount being underestimated by 9 to 11 percentage points. Besides investigating a blind-zone of 1200 m, the impacts of a reduced blind-zone of 600 m are also analyzed. This analysis will help in assessing future missions with a smaller blind-zone. The reduced blind-zone leads to improved representation of mean reflectivity but does not improve the bias in event numbers and precipitation amount.

1. Introduction

As an integral part of the water cycle in polar regions, snowfall is extremely difficult to capture at the relevant spatial scale and with sufficient accuracy [*Levizzani et al.*, 2011]. Surface observations by in-situ sensors are sparse and available only over land [*Schneider et al.*, 2014], and snowfall measurements in polar regions are particularly affected by wind induced errors such as under-catch or over-catch from blowing snow [*Yang et al.*, 1999; *Knuth et al.*, 2010].

An important source of spatially extensive measurements of snowfall are remote sensing observations from space, such as microwave radiometer [*Levizzani et al.*, 2011] or the radar of the CloudSat satellite [*Stephens et al.*, 2008]. CloudSat allowed snowfall climatologies for polar regions up to 82° N/S to be derived for the first time [*Liu*, 2008a; *Kulie and Bennartz*, 2009; *Palerme et al.*, 2014]. However, accurately determining the snowfall rate (S) from the observed profile of the equivalent radar reflectivity factor (Z_e) is challenging due to the microphysical and microwave scattering uncertainties in the conversion of Z_e to S [e. g., *Hiley et al.*, 2011] and the inability to reliably measure Z_e close to the surface when using satellite radar systems. Our research addresses this latter point by studying how this "blind-zone" affects observations and what impact a reduced blind-zone would have.

The vertical extent of this blind-zone is largely determined by the surface type and is smaller over the ocean and larger over land or sea ice [*Durden et al.*, 2011a]. For CloudSat, it has been shown that, over land, the received signal is free from ground clutter only from the fifth range bin above ground level (1200 m agl, hereafter $H_{\mathrm{CS}} = H_{\mathrm{CloudSat}}$) [*Marchand*

et al., 2008]. New space-borne radars such as the recently launched dual frequency radar on-board the Global Precipitation Measurement (GPM) Core Observatory [*Hou et al.*, 2014] or the Cloud Profiling Radar (CPR) on-board the upcoming Earth Clouds, Aerosols and Radiation Explorer (EarthCARE) mission [*Gelsthorpe et al.*, 2010; *Donovan et al.*, 2013] are expected to achieve smaller blind-zones ranging between 600m and 1000m above surface (depending on radar operation mode). Other proposed missions such as the Polar Precipitation Measurement Mission [*Joe et al.*, 2010] or the Aerosol/Cloud/Ecosystems (ACE) mission [*Durden et al.*, 2011b] are heading to blind-zones in the order of 100 to 200 m.

These observational blind-zones are likely to introduce errors in the derived statistics of snowfall frequency and S for surface level if the snowfall properties are significantly altered within the blind-zone. For example, snowfall might be underestimated or completely missed, if the snow cloud is shallow. The opposite extreme of snowfall overestimation would be snowfall that is detected at the top of the blind-zone but completely sublimates on its way down to the surface. Besides these extreme scenarios, the snowfall properties observed at the top of the blind-zone might also be altered within the blind-zone due to microphysical processes or wind shear. For mid-latitude systems, a general increase of the radar reflectivity factor towards the ground in the range of 3 to 7 dB km^{-1} was found and has been associated to aggregation and depositional growth [*Fabry and Zawadzki*, 1995; *Liu*, 2008a; *Matrosov and Battaglia*, 2009; *Wolfe and Snider*, 2012]. While there is large variability, reflectivity gradients are found to generally increase with higher temperatures. *Henson et al.* [2011] and *Stewart et al.* [2004] studied ground-based radar data for the Canadian Arctic region and found radar reflectivity in the lowest 2 km above ground to

be nearly constant. However, some cases revealed increasing as well as decreasing radar reflectivities in the range of 5 dB km^{-1} towards ground depending on the thermodynamic structure of the lowest layers and the intensity of snowfall. Despite its blind-zone limitations, CloudSat still detects significantly more light snowfall than the ground-based precipitation radar networks do because of its higher sensitivity [*Smalley et al.*, 2014].

The goal of this paper is to investigate the impact of the blind-zone on snowfall statistics at three polar sites and to estimate whether statistics derived from observations above the blind-zone are biased in comparison to statistics taken at the surface. One way of investigating the impact of the blind-zone is to directly compare CloudSat overpasses over a site where the lower reflectivity profile is measured with results from a ground-based cloud radar. However, these direct comparisons can be strongly affected by the difference in observed radar volumes or the horizontal displacement of the satellite overpass from the location of the ground-based radar. These complications can be avoided by statistically comparing satellite and ground-based radar observations [*Protat et al.*, 2009, 2010]. Alternatively, variations of radar reflectivity within the blind-zone using only ground-based observations can be investigated. We use the observations at the top of the blind-zone from the ground-based radars as a reference for the statistics that a theoretically perfect overpassing and volume matched satellite radar would provide. In this way, we avoid any approximation due to temporal, spatial or radar volume mismatch while the generally expected changes (e. g., under-/overestimation of snowfall) within the blind-zone are assumed to appear in both the real satellite observations and the ground-based measurements.

In this study, we apply this method to long-term radar observations from observational sites in Antarctica and Svalbard. These ground-based observations were carried out using the Micro Rain Radar (MRR), a compact and lightweight 24 GHz frequency modulated continuous wave (FMCW) radar [*Klugmann et al.*, 1996].

2. Study area

We use column measurements from the Princess Elisabeth Station (PE) in East Antarctica and from Ny-Ålesund (NÅ) and Longyearbyen (LY) in Svalbard, Norway as exemplary datasets for polar regions. To the authors knowledge, no other ground-based precipitation radar is currently operating in Antarctica and the datasets from NÅ and LY are the first of their kind in Svalbard. Because the setup and the results in LY were similar to NÅ and both sites are only 110 km apart, results for LY are only presented in the supplementary material. Nevertheless, comparison of both sites is important when assessing how representative the study is.

2.1. Princess Elisabeth Station, East Antarctica

The only current precipitation radar over the Antarctic ice sheet is installed as part of the meteorological-cloud-precipitation observatory that has been operating at the PE station since February 2010 [*Gorodetskaya et al.*, 2014a] (http://ees.kuleuven.be/hydrant). The station is built on Utsteinen Ridge located north of the Sør Rondane mountains in the eastern part of Dronning Maud Land (DML) at the ascent to the East Antarctic plateau (71°57' S, 23°21' E, 1392 m amsl, 173 km from the coast, Fig. 1.a). Together with other remote-sensing instruments, the MRR precipitation radar is installed on the roof of the PE station about 10 m above the snow surface (Fig. 2.a). An automatic weather station

providing meteorological data is located 300 m east of the PE base [*Gorodetskaya et al.*, 2013]. In this study, we use year-round measurements available for the full year 2012.

The PE site is characterized by a relatively mild climate, mainly due to the favorable location for warm air advection associated with local intense cyclonic activity and a lack of drainage of cold air from the high plateau due to shelter from the Sør Rondane Mountain [*Gorodetskaya et al.*, 2013]. Two main meteorological regimes govern the weather at PE—the cold katabatic regime and the warm/transitional synoptic regime [*Gorodetskaya et al.*, 2013]. The katabatic regime is characterized by low wind speeds of predominantly south-southeasterly direction, strong near-surface temperature inversions, low specific humidity, and low incoming longwave fluxes indicative of clear skies. The synoptic regime at PE is in turn associated with the Southern Ocean cyclones passing near DML and bringing heat and moisture advection into the Antarctic ice sheet [*Noone et al.*, 1999; *Schlosser et al.*, 2010]. Precipitation at PE (only as snowfall) mainly occurs during synoptic regimes. The largest snowfalls observed at PE have been associated with narrow bands of enhanced moisture amounts ("atmospheric rivers") directed into DML and surrounding sectors [*Gorodetskaya et al.*, 2014b]. Such rare large snowfall events contribute significantly to the total yearly snow accumulation and can explain the high inter-annual variability of snow accumulation at the PE site (from 23 up to 230 mm water equivalent per year [*Gorodetskaya et al.*, 2014a, b], and entire DML [*Boening et al.*, 2012; *Lenaerts et al.*, 2012].

2.2. Ny-Ålesund, Svalbard

Measurements in the Arctic were taken in NÅ (78.92°N, 11.93°E, 8 m amsl) on Spitsbergen, the largest island of the archipelago of Svalbard, Norway (Fig. 1.b). The climate

in Svalbard is strongly influenced by the West Spitsbergen Current, which flows from the North Atlantic along the west coast of Spitsbergen and provides the largest input of sensible heat into the Arctic Ocean [e. g., *Gammelsrød and Rudels*, 1983]. Through mixing, some of this heat reaches the fjords in the west of the island and leads to a much milder climate than in other locations at the same latitude (e. g., Greenland). Additionally, Svalbard lies in the North Atlantic storm track with general cyclogenesis and rapid cyclone deepening within the Icelandic Low and penetrating into the Arctic [*Serreze et al.*, 1997; *Tsukernik et al.*, 2007]. As a consequence, the atmospheric influence on the climate varies between moist and warm air masses coming from the Atlantic and dry and cold air masses coming from the Arctic. Precipitation in Svalbard can therefore be liquid as well as solid.

Ny-Ålesund lies at the shore of the Kongsfjord, which is 26 km long and up to 14 km wide. This position leads to a maritime climate, when the fjord is ice-free, and higher precipitation, with an annual mean of 427 mm (for the period 1981-2010), than in the interior of Spitsbergen [*Førland et al.*, 2012]. The MRR was placed on the roof of the Sverdrup Research Station operated by the Norwegian Polar Institute (NP) in 8 m agl height (Fig. 2.b), 350 m away from the sea. Standard meteorological observations are taken from the weather station of the Norwegian weather service (WMO no. 01007, data available at http://eklima.met.no) located 100 m south-east of the NP-station. Measurements were taken over a period of one year between 10th of March 2010 and 15th of March 2011.

2.3. Regime Classification

To investigate whether the impact of the blind-zone on snowfall measurements depends on the type of snow event or ambient weather conditions such as stability or humidity, the

dataset is classified into different regimes. Sublimation of precipitation before reaching the surface (virga phenomenon) depends both on precipitation microphysical properties (such as particle size and terminal velocity) and on the ambient meteorological conditions [*Clough and Franks*, 1991; *Wang et al.*, 2004; *Campbell and Shiobara*, 2008; *Evans et al.*, 2011]. Dry meteorological conditions with a relatively warm sub-cloud layer will favor virga formation, whereas saturated and mixed sub-cloud layer will favor precipitation to the surface. The occurrence of either conditions was identified based on the classification of 3-hourly measurements of low-level temperature inversion (T_{inv}) and near-surface relative humidity with respect to ice (RH_i) in the vicinity of PE and NÅ stations.

Near-surface T_{inv} (°C m^{-1}) is calculated as the difference between the air temperature and the skin surface temperature of snow. The air temperature is measured at the variable height (within 2 - 4 m) above the snow surface depending on snow accumulation. Surface temperature is calculated using measurements of outgoing and incoming long-wave radiative fluxes (see *Gorodetskaya et al.* [2013] for details).

Prior to regime classification, the data were deseasonalized and standardized by subtracting monthly mean values and calculating z-scores; the classification is based on hierarchical cluster analysis of RH_i and T_{inv} following *Gorodetskaya et al.* [2013]. Two main regimes were identified: the *dry stable regime* characterized by low RH_i and high T_{inv}, which represents 27% (41%) of all observations at PE (in NÅ), and for all other events the *wet unstable regime* with high RH_i and near-zero T_{inv}. MRR observations are grouped according to the two regimes. The regime classification was not applied to the dataset in LY because no weather station was available in the immediate vicinity.

3. Radar observations of snowfall

In this study, MRR data are used to mimic CloudSat measurements (Table 1) while investigating how radar observations are altered in the blind-zone.

3.1. CloudSat

CloudSat, which is part of the A-train satellite constellation, carries the Cloud Profiling Radar (CPR) operating at a frequency of 94.05 GHz ($\lambda = 3.2$ mm) [*Stephens et al.*, 2008; *Tanelli et al.*, 2008; *L'Ecuyer and Jiang*, 2010]. The raw measured return power is provided in the level 1 data product (1B-CPR) and converted into equivalent attenuated reflectivity factor, included in the 2B-GEOPROF data product [*Tanelli et al.*, 2008]. Near the surface, the reflectivity product is contaminated by ground clutter leading to significant power returns not related to hydrometeor occurrence [*Marchand et al.*, 2008; *Tanelli et al.*, 2008]. Although the latest 2B-GEOPROF version has a clutter reduction procedure, this procedure is less effective over land than over ocean and is particularly ineffective over mountainous terrain [*Mace*, 2006]. Consequently, snowfall rates at the surface derived from truncated 2B-GEOPROF profiles need to be approximated by snowfall rates at an elevated height of 1200 m (H_{CS}) above the surface, introducing an effective blind-zone of 1200 m agl over land. To ensure equal processing of MRR and CloudSat (see Sec. 3.3), Z_e data of the 2B-GEOPROF product are used even though a CloudSat snowfall product [2C-SNOW-PROFILE *Wood*, 2011; *Wood et al.*, 2013] based on 2B-GEOPROF has recently been released. CloudSat is said to be overpassing a station if its nadir view is within a radius of 100 km. Based on this radius, we found 899 overpasses for the PE study area and 1,579 overpasses for the NYA study area in the period between 2006

and 2013. Reflectivities of the lowest clutter-free range gate at H_{CS} as reported by the 2B-GEOPROF product are analyzed for each overpass.

3.2. Micro Rain Radar

The MRR (Micro Rain Radar) is a vertically pointing Frequency Modulated Continuous Wave (FMCW) radar manufactured by METEK GmbH, Germany [*Klugmann et al.*, 1996] operating at a frequency of 24 GHz ($\lambda = 1.24$ cm). Its low power consumption of only 25 W makes it particularly suitable for remote areas with limited power supply. The MRR was originally developed to measure rain [*Peters et al.*, 2002, 2005; *Tridon et al.*, 2011], but recent modifications in the MRR data processing [*Maahn and Kollias*, 2012] and comparisons to cloud radar observations [*Kneifel et al.*, 2011] have revealed that the MRR can also be used to study snowfall [*Stark et al.*, 2013; *Gorodetskaya et al.*, 2014a].

The MRRs were equipped with a 200 W antenna heating, but the heating was only used in NÅ when temperatures were around the melting point. At lower temperatures, the heating is unable to completely melt the snow, which causes the dish to glaciate resulting in a disturbance of the measurements. Presence of a thin layer of dry snow, instead, does not contaminate the measurements because attenuation by dry snow is very weak at K-band [*Matrosov*, 2007] and the snow is easily blown away by the ambient wind before a large layer can accumulate. The antenna dish of the MRR in NÅ was checked daily by the station staff to avoid glaciation of the dishes. The MRR at PE was regularly checked by the staff in summer and additionally supervised via webcam to check the status of the instrument during the unmanned period.

The MRR provides data at 31 range gates with a resolution of 100 m agl (60 m agl) at PE (in NÅ). The first two and the last range gate are extremely noisy and removed from

the analysis. Because MRR's original software was designed for rain only, the alternative software package IMProToo designed for observations of snowfall by *Maahn and Kollias* [2012] has been used for this study. Due to the fixed MRR Doppler velocity range of 0 to 12 m/s, aliasing effects might occur at upward or very low fall velocities (as is common for snow). These effects can be corrected by IMProToo for all but the third MRR range bin [see *Maahn and Kollias*, 2012, for details]. Therefore the third bin has also been excluded from the analysis so that an effective measurement range of 400 to 3000 m agl for PE (240 to 1800 m agl for NÅ) remains. Hereafter, the altitude of the lowest observation of the MRR will be called $H_{\mathrm{SF}} = H_{\mathrm{SurFace}}$. A contamination of the measurements due to blowing snow is unlikely at H_{SF} and above [*Xiao et al.*, 2000].

To increase MRR's sensitivity to around −10 dBz (−12 dBz) at PE (in NÅ), MRR data were averaged to 300 s. Even though this averaging reduces temporal and horizontal resolution (due to stronger advection effects), this reduction is justified as convective events with high temporal variability are rare at polar sites. Unfortunately, MRR's noise level varies significantly between different instruments and can vary by more than 5 dB in time, which leads to temporary lower sensitivities. To exclude the impact of a varying sensitivity on the presented analyses, MRR data with $Z_e < -5$ dBz is discarded. This Z_e value corresponds to 0.02 to 0.09 mm/h depending on how Z_e varies with snowfall rate (see Sec. 3.3)

To exclude rainfall events in Svalbard from the analysis, data from temperatures above −2 °C were removed. Note, that liquid precipitation events were used to verify the calibration of the MRR by comparing it with the reflectivity measured by an optical PARSIVEL disdrometer [*Löffler-Mang and Joss*, 2000]. No significant offset was found, so the calibra-

tion of the MRR in NÅ is expected to be correct within ±1 dB. No calibration reference is available for PE, but a calibration offset would only affect absolute values and not the profile structure.

3.3. Estimating precipitation rates from radar measurements

To convert the equivalent radar reflectivity factor Z_e into snowfall rates S, a power law relation is usually used:

$$Z_e = a \cdot S^b. \tag{1}$$

The parameters a and b depend on several assumptions e. g., on the assumed particle habit, density, orientation, and particle size distribution. Backscattering properties of snow particles are increasingly affected by non-Rayleigh effects if the snowflake size is in the range of the radar wavelength. In addition, the natural variability of snowfall properties introduces a large uncertainty for any Z_e-S relation. Most Z_e-S relations for cloud radars have been derived for 35 GHz or 94 GHz, but not for 24 GHz. Calculations using an extended and updated version of the scattering database for snow particles [*Liu*, 2008b] revealed that the difference between backscattering at 24 GHz and at 35 GHz is below 0.5 dB and hence, the 35 GHz Z_e-S relation is applied to MRR observations at 24 GHz in this study. Note that *Kneifel et al.* [2011] came to a different result because of interpolation effects across frequency: at that time, the database of *Liu* [2008b] did not include scattering estimations for 24 GHz.

To take the uncertainty of a Z_e-S relation into account, we use three Z_e-S relations from *Kulie and Bennartz* [2009], which are available for both 94 and 35 GHz (Table 2). These relations have been derived from aircraft measurements of particle size distribution

and a large set of snow particle habits and their associated scattering properties. While the conversion of Z_e to S is necessary to illustrate the impact on snow amount at the surface, most analyses are performed in Z_e-space in order to confine uncertainties to the vertical structure.

Note that due to increasing non-Rayleigh effects with increasing particle size, Z_e measured by MRR can be larger than that measured by CloudSat. To estimate this effect, a correction term

$$Z_{e\,(94\,\mathrm{GHz})} = \alpha \cdot Z^{\beta}_{e\,(35\,\mathrm{GHz})} \tag{2}$$

is derived by solving each pair of 35/94 GHz Z_e-S relations presented above for S (see Table 2). In Fig. 3, the resulting differences for a Z_e range of -10 to 30 dBz are presented. It shows a significant decrease of Z_e with a high spread due to particle type. For example, an MRR measurement of 10 dBz corresponds to Cloudsat measurements between 1.38 and 7.66 dBz. In the following, the conversion for aggregates is used as an average of the different relations.

4. Comparison of MRR and Cloudsat above the blind-zone

For our assumption that the MRR observations below the blind-zone can be used to investigate the changes in Z_e within Cloudsat's blind-zone, we first have to investigate whether MRR generally reproduces the Z_e statistics measured by CloudSat above the blind zone. Because Z_e from both instruments cannot be directly compared due to the different radar frequencies, the comparison is performed in terms of S using the Z_e-S relations introduced in Sec. 3.3.

For this, we also applied the MRR sensitivity threshold to CloudSat data. The −5 dBz threshold of the MRR corresponds to −7.10 dBz at 94 GHz assuming aggregates for Eq. 2 (−8.97 dBz for snow, −6.25 dBz for three bullet rosettes). In comparison to the snowfall threshold of −10 dBz defined by *Liu* [2008a], this threshold reduced the number of events by 6 to 24%, depending on assumed particle type. Because these events only weakly contribute to total precipitation, snow mass is only reduced by 1 to 5%. Consequently, we can assume that the MRR is able to capture the majority of snowfall.

The comparison of the frequency distributions of derived snowfall rate S at H_{CS} for both PE and NÅ stations (Fig. 4) reveals the generally strong similarity between CloudSat and MRR data at H_{CS} despite the different radar and data sampling characteristics. However, some differences between the CloudSat and MRR snowfall rate distribution occur particularly at PE, where CloudSat shows a broader frequency distribution shifted to higher S. Note that this discrepancy disappears if the MRR data are modified by an assumed calibration offset of +2 dB. Although we are currently unable to properly correct the calibration for the MRR at PE, such a constant bias would not affect the results of this study since we are using the same instrument for different heights and only analyze their relative differences. Attenuation effects might also lead to an offset between CloudSat and MRR because attenuation at 94 GHz is one order of magnitude larger than at 35 GHz, as shown by *Matrosov* [2007]. However, they found that attenuation is only relevant for higher precipitation rates and thick snow layers, where attenuation can exceed 1 dB. In addition, attenuation is partly compensated for by multiple scattering effects in heavier snowfall [*Matrosov and Battaglia*, 2009]. Attenuation due to supercooled liquid water can

be neglected at 24 GHz and is below 1 dB at 94 GHz for liquid water paths of less than 100 g m^{-2} [e. g. *Kneifel et al.*, 2014].

Further, the wide range of occurrences for a specific S (e. g., between 0 - 5% for S = 1 mm hr^{-1} for CloudSat at PE) demonstrates that the uncertainty in S due to the use of different $Z_e - S$ relationships associated with varying snow microphysical characteristics is much larger than the difference between MRR and CloudSat data.

5. Analysis of the blind-zone

Based on our comparison of MRR and CloudSat at H_{CS} in the previous section, we can assume that the MRR observations within CloudSat's blind-zone can be used to investigate the impact of the blind-zone on snowfall frequency and snowfall rate estimation. In the following, we will also include a blind-zone height of 600 m ($H_{\mathrm{FM}} = H_{\mathrm{FutureMission}}$ hereafter) in the analysis. This height represents the most optimistic estimation of the blind-zone of future satellite missions.

The different possible errors introduced by assigning the reflectivities at H_{CS} to the surface level can be identified in Fig. 5 showing example days of the observed, rather complex but typical, precipitation structures. In the example at PE (Fig. 5.a), two precipitation layers can be identified during the day. They appear to be disconnected when observed with an MRR: a high precipitation layer with high Z_e values, does not necessarily imply that precipitation reaches the ground. For the NÅ case (Fig. 5.b), the effect of sublimating precipitation or virga is even more pronounced with precipitation sometimes reaching surface levels but most of the time sublimating aloft. Consequently, in these cases, the blind-zone would lead to an overestimation of snowfall on the surface (hereafter referred to as *commission error*). At PE the opposite effect can also be seen: shallow

precipitation that would be potentially missed by a satellite radar and thus resulting in an underestimation of snowfall on the ground (hereafter called *omission error*).

In the following subsections, we analyze the ground-based datasets, focusing on different aspects: what is the impact of the blind-zone on the climatology of observations in respect to 1) Z_e distribution, 2) number of events and 3) single events? Finally, we discuss the effect of the blind-zone by considering precipitation amount.

5.1. Impact on Z_e distribution

In the following, we investigate whether the vertical distribution of Z_e is affected by virga, shallow precipitation or microphysical processes such as sublimation, riming and aggregation. For this investigation, reflectivity vs. altitude 2D histograms (2DH) of observed reflectivities for the complete observation period of one year are shown in Figs. 6.b and 7.b for PE and NÅ, respectively. To enable a better interpretation of the MRR statistics in terms of CloudSat observations, results are shown for both, 24 GHz Z_e and converted to 94 GHz assuming aggregates (see Fig. 3 for the impact of assuming other snow types). For both sites, the 2DH is very homogeneous between H_{SF} and H_{CS}. The median of reflectivity is constant with altitude in NÅ and shows only a weak increase of 1-2 dB towards the surface at PE. This low reflectivity gradient is highly consistent with the findings of an almost constant Z_e profile found in *Henson et al.* [2011] for the Canadian Arctic.

The distribution of reflectivity measurements at H_{CS} and H_{SF} is also compared using Detrended Quantile-Quantile (DQQ) [*Thode*, 2002] plots (Figs. 6.c and 7.c). For this, both series of Z_e are divided into n_Z quantiles where n_Z is the length of the shorter Z_e series. Then, the quantiles are sorted and the quantiles of H_{CS} and H_{SF} are subtracted

from each other. This difference of quantiles is plotted against the quantiles for Z_e at H_{SF}. By this, the distribution of Z_e at H_{CS} can be directly compared to the distribution at H_{SF} and even small differences between these distributions become visible. In contrast to the analysis of vertical gradients of individual profiles, this method has the advantage that it is not influenced by changes of the Z_e profile due to e. g., advection or temporal evolution. For PE, the distribution of Z_e at H_{CS} is shifted towards smaller reflectivities by a maximum of 2.3 dB in the medium Z_e range. The agreement of distributions increases for Z_e values larger than 10 dBz, indicating more similar distributions for stronger events. However, due to the relatively small number of events in this high-reflectivity region, a more extended dataset would be necessary for a clear conclusion. For NÅ, agreement of Z_e distributions is better, and the shift between distributions at H_{CS} and H_{SF} is mostly below 1 dB, often below 0.5 dB with a slight increase towards larger Z_e. Performing the comparison with MRR data converted to 94 GHz has only minor impact on the results.

To investigate whether the found changes in statistics depend on the regime classification, the analysis is repeated for the two synoptic regimes. For the *wet unstable regime* (Figs. 6.e, f and 7.e, f), only small differences to the complete dataset are visible in the 2DH and the DQQ-plot. However, the *dry stable regime* (Figs. 6.h, i and 7.h, i) features, on average, lower reflectivities for both sites, especially at the levels below H_{CS} because moisture supply for particle growth in the near-surface layers is low while temperatures are relatively high, favoring particle sublimation. In NÅ, the distribution of Z_e at H_{CS} is shifted by up to -1 dB in comparison to H_{SF} for the *dry stable regime*, which is probably related to sublimation effects (Fig. 7.i). For PE, the shift of the distribution is similar to

the one using the complete dataset—except for rare values exceeding 10 dBz. Sublimation effects lead to a reduction of the shift of Z_e distributions by 0.3 dB (Fig. 6.i).

To investigate the impact of a reduced blind-zone, DQQ-plots are also presented for an observation height of 600 m agl (H_{FM}, Figs. 6.c, f, i and 7.c, f, i). For NÅ, this results in a significantly better statistical agreement of H_{FM} and H_{SF}. The offset is only ± 0.5 dB for all regimes. For PE, the agreement of Z_e distributions is improved and the offset of the distributions is below ± 1 dB and only for the *dry stable regime* (Fig. 6.i) is the offset negligible and below ± 0.5 dB. In summary, a reduction of the blind-zone by 50% significantly improves the agreement of the Z_e distributions at H_{SF} and the observation altitude. We expected the impact on Z_e distribution to still be underestimated for H_{CS} and H_{FM} at PE because H_{SF} is at an altitude of 400 m agl and processes between the surface and H_{SF} are not considered. In NÅ, H_{SF} is at 240 m agl, so the underestimation is expected to be less. The results for LY, which are very similar to NÅ, can be found in Fig. S.1 of the supplementary material.

5.2. Impact on the number snowfall events

To investigate the impact of the blind-zone on the total number of observed precipitation events, N—defined as the number of observations greater than -5 dBz—is calculated as a function of height (Figs. 6.a and 7.a). By restricting the number of events in one height to those with snowfall at H_{CS} ($\hat{N}$ in Figs. 6.a, 7.a), the number of shallow events (omission error, N_{OM}) can be estimated by the difference between N and $\hat{N}$. At PE (NÅ), 38.7% (34.1%) of 7,153 (7,537) observations are classified as omission errors because they are present at H_{SF} but not at H_{CS} above. For PE, this number might even be too low if shallow events occur below H_{SF} of 400 m agl.

Virga events that sublimate and do not reach H_{SF}, although they are present at H_{CS} (commission error, N_{CM}), can be estimated by the decrease of $\hat{N}$ relative to its maximum at H_{CS}. As a result, 44.4% (28.9%) of the events observed at H_{CS} do not reach the surface at PE (in NÅ). So N_{OM} is similar for PE and NÅ, while N_{CM} is not.

It is important to note that N_{OM} and N_{CM} not only contain shallow and sublimating precipitation events but are also affected by advection and shear effects as well as by the terminal fall velocity of snow, which also causes slanting of the observed snowfall profiles. When a cloud starts to precipitate, particles need up to 20 minutes from H_{CS} to the surface assuming a mean fall velocity for snow of $1\,\mathrm{ms}^{-1}$. During these first 20 minutes, the event will be classified as a commission error. On the other hand, if the cloud stops precipitating, the last 20 minutes of the event will be classified as an omission error. Although N_{CM} and N_{OM} might be overestimated, they are affected in the same way in the long-term. Thus, the difference between both errors is expected not to be biased by the slanting of the profiles. If advection of precipitation is assumed to be homogeneously distributed, advection effects are also expected to cancel each other out.

The difference between N_{OM} and N_{CM} is equal to the difference of N between the altitudes at H_{CS} and H_{SF}. For PE, N is reduced by 5.7% from H_{CS} towards the surface (Fig. 6.a). In contrast, N increases by 5.2% at the surface for NÅ (Fig. 7.a). Interestingly, the increase towards the surface is not monotonic, but the vertical distribution of N is "belly shaped" with a maximum at H_{FM}. Since the decrease towards H_{SF} is smaller than the increase to H_{CS}, a net increase of N occurs at NÅ. In other words, at PE, virga events are more frequent than shallow precipitation (Fig. 6.a) whereas at NÅ, shallow precipitation occurs more frequently (Fig. 7.a).

In NÅ, the maximum occurs at H_{FM}, which implies that a reduced blind-zone with H_{FM} would lead from an underestimation of N to an overestimation by 17.8%. For PE, the overestimation of N would only slightly change from 5.7% to 8.5%. This deterioration is in contrast to the finding that the statistical representation of Z_e is improved for a lower blind-zone (Figs. 6.c, 7.c). Apparently, the combination of virga and shallow precipitation leads to a local maximum of occurrence between H_{FM} and H_{CS}.

While there is a clear tendency towards larger N below H_{CS} for the *wet unstable regime* indicating more frequent shallow precipitation (Figs. 6.d, 7.d), a stronger decrease of snow events can be observed for the *dry stable regime* at both sites (but more pronounced at PE, Figs. 6.g, 7.g). This stronger decrease might be attributable to strong sublimation and virga formation.

5.3. Impact on individual snowfall events

While the previous sections investigated the mean occurrence of snow characteristics, we now highlight the large spread if single events are considered. This procedure is important because the 16-day repeat cycle of CloudSat means that a particular precipitation event is usually only observed once and temporal evolution cannot be measured. For this investigation, we sort the profiles with respect to their Z_e values at H_{CS}; the resulting 2DH diagrams for the different Z_e intervals at H_{CS} are shown in Fig. 8 for PE and Fig. 9 for NÅ for the original measurement and also converted to 94 GHz. While events with Z_e of up to 7 dBz at H_{CS} tend to increase towards the surface on average by 0.5 to 3 dB, events with larger Z_e decrease by up to 3 dB. Transferred to a CloudSat observation, this result means that CloudSat would tend to underestimate weaker precipitation events while it

would overestimate stronger events. This finding also holds for LY, and the corresponding plot can be found in the supplementary material (Fig. S.2).

While for lower Z_e up to 3 dBz, this finding is consistent with our findings in Sec. 5.1, for higher Z_e, an analysis of the DQQ-plots revealed a shift of the Z_e distribution to higher reflectivities at H_{CS} in comparison to at H_{SF} (Figs. 6.c, 7.c). This result highlights the vertical inhomogeneity of precipitation events at a single time-step and it can be also seen in the large spread of observations at H_{SF} for a single Z_e interval being larger for NÅ than for PE.

5.4. Impact on the total mass flux

The hydrological cycle is driven by the flux of precipitation to the surface. To investigate the impact of the blind-zone on mass flux, Fig. 10 presents an estimation of the snowfall rate profile for PE and NÅ. The figure reveals how the different reflectivity values contribute to the total precipitation as a function of height using the $Z_e - S$ relation for *snow* presented in Sec. 3.3. The total liquid equivalent snowfall amount of the 12-month dataset derived from MRR is roughly 200 mm at PE and 320 mm in NÅ, although uncertainty of the absolute values is large due to the application of the $Z_e - S$ relation. Hence, we normalized the precipitation amount at every height with respect to the total precipitation amount at H_{SF}, resulting in a reduced sensitivity of the precipitation amount profile to uncertainties in the $Ze - S$ relation.

The vertical changes of Z_e are a combination of changes in the reflectivity distribution (Sec. 5.1) and the variation of N with height (Sec. 5.2). In general, events with reflectivities between 0 and 10 dBz (corresponding to 0.2 and 0.7 mm/h, respectively, using the Z_e-S relation for *snow*) contribute most to the total precipitation amount at PE (Fig. 10.a),

underlining the need for a high radar sensitivity. This finding is in agreement with the results from *Kulie and Bennartz* [2009], who found that most precipitation in the northern periphery of Antarctica originates from precipitation rates of 0.2 to 1 mm/h, and indicates that our dataset is typical for Antarctica. Events with reflectivities larger than 15 dBz are so rare that they hardly contribute to the total precipitation amount. The contribution of the various classes of reflectivity is different for NÅ (Fig. 10.b): most precipitation originates from events with reflectivities between 15 and 20 dBz, which is related to the, on average, warmer and moister climate in Svalbard.

The vertical development of the different reflectivity classes shows how behavior is different for NÅ and PE. For PE, the contribution of the 0 to 5 dBz interval and the 10 to 15 dBz interval changes little for the height between H_{CS} and H_{SF}. The contribution of the 5 to 10 dBz interval, however, increases towards the surface. At PE, the total mass flux at H_{CS} is underestimated by 11 percentage points of total precipitation in comparison to H_{SF}. At H_{FM}, this changes to an overestimation of 3 percentage points, but uncertainty is high because, for PE, observations below 400 m are not available and the further development towards the ground is unknown.

In NÅ, the contribution of the three intervals between 5 and 20 dBz is even more similar at H_{CS} and H_{SF}. For the range between H_{CS} and H_{SF}, however, all reflectivity intervals larger than 5 dBz contribute more to the total precipitation than at H_{CS} and H_{SF}. Apparently, omission and commission errors are competing, but cancel out each other close to the surface. This result would also mean that a future satellite based radar mission with a smaller blind-zone would not improve the estimation of the total mass flux. Instead, at least for NÅ, total mass flux would be overestimated by 19 percentage points—in com-

parison to 9 percentage points underestimation at H_{CS}. The results are similar for LY (see supplementary material Fig. S.3) and prove that the belly-shaped distribution is not a local effect.

These results are robust as demonstrated by using again the two other $Z_e - S$ relations introduced in Sec. 3.3 to estimate the uncertainty. As can be seen from Fig. 10, applying a different $Z_e - S$ relation has only a minor effect on the results and does not change the overall shape of the distribution. Even if the $Z_e - S$ relation changes with height, the impact on the total precipitation distribution is less than 5%.

6. Summary and Conclusion

The impact of CloudSat's blind-zone below 1200 m agl (H_{CS}) on snowfall statistics was investigated for three polar sites, the Belgian Princess Elisabeth Station (PE) in East Antarctica, and for Ny-Ålesund (NÅ) and Longyearbyen (LY, see supplementary material for results) in Svalbard, Norway (Fig. 1). To investigate the impact on a future satellite mission with a reduced blind-zone, a blind-zone of 600 m agl (H_{FM}) was also considered.

We used a ground-based Micro Rain Radar and compared with the lowest clutter-free CloudSat observation height H_{CS} (Fig. 4). The MRR was found suitable because differences due to the different footprint and temporal resolution were found to be less than the uncertainty caused by the applied $Z_e - S$ relation. Consequently we investigated the blind-zone effects by comparing MRR observations at H_{CS} with MRR observations near-surface (H_{SF}), assuming that MRR observations are representative of CloudSat observations. To our knowledge, the 12-month MRR datasets from NÅ and LY are the first precipitation radar observations available for Svalbard. The MRR at PE is currently the only ground-based precipitation radar in Antarctica.

The frequency distribution of MRR reflectivity changes between H_{CS} and H_{SF} . For PE (Fig. 6.c), the distribution of Z_e is shifted by up to 2.5 dB towards smaller values if measured at H_{CS}. For NÅ (Fig. 7.c), the shift is much smaller and below 1 dB. A reduction of the blind-zone by 50% leads to a reduction of the offset by more than a factor of two for PE, and in NÅ the remaining shift is negligible.

The better agreement due to a reduction of the blind-zone cannot be seen when analyzing the total number of observations N (Figs. 6.a and 7.a): at H_{CS}, N is overestimated by 5.7% and underestimated by 5.2% for PE and NÅ, respectively. At H_{FM}, this result changes to over-estimations of N of 8.5 and 17.8%. This change is more strongly pronounced at NÅ and most likely due to competing processes: virga and shallow precipitation.

Based on temperature inversion and relative humidity, the dataset was divided into two regimes: the *dry stable* and the *wet unstable regime*, with the latter representing 73% and 59% of all precipitation events at PE and NÅ, respectively. For the *dry stable regime*, the overestimation of N at H_{CS} and H_{FM} is most pronounced and Z_e decreases towards the ground, i. e., virga effects dominate, as might be expected due to increased sublimation. For the *wet unstable regime*, agreement of N at the different levels is better. This indicates that, for these regimes, which are more related to the influence of synoptic disturbances, the profiles are on average slightly more constant in the vertical. This classification might be exploited for mitigation strategies.

Agreement of observations between H_{CS} and H_{SF} is less when single events are considered (Figs. 8, 9) because precipitation intensity strongly varies with height due to the fall

velocity of ice particles and due to advection effects. Hence, low precipitation intensity gets generally enhanced and high precipitation intensity becomes generally weaker.

The change in both, N and Z_e contributes to the estimation of precipitation amount (Fig. 10). For NÅ, the belly shape of N can be also seen in the total precipitation amount: at H_{CS}, total precipitation is underestimated by 9 percentage points while at H_{FM}, it would be overestimated by 19 percentage points, which is mainly driven by events with $Z_e >$ 15 dBz. For PE, such a belly shape cannot be clearly seen, but the underestimation of total precipitation of 11 percentage points at H_{CS} still changes to an overestimation of 3 percentage points at H_{FM} showing that virga and shallow precipitation effects are also partly overlapping at PE.

In general, our results are only valid for the vicinity around the station. However, due to the spatial homogeneity of surface properties in East Antarctica we expect our findings to be representative of a much larger area. For Svalbard, orography is much more complex, limiting the spatial representativeness of this study. Because results for an identical setup in LY, located 110 km south-east of NÅ, are comparable (see supplementary material), we are nevertheless confident that our results are representative at least for the western region of Svalbard.

In summary, shallow precipitation and virga effects are found to compete and lead to a change in the number of observed events and total mass flux of 9 to 11 percentage points, although the statistical distribution of Z_e changes only little. While the statistical agreement is enhanced with a potentially lower blind-zone altitude, the difference in the number of observed events and total mass flux increases. Hence, a reduced blind-zone would not improve snowfall observations in all aspects.

For the future, more radar observations would allow further investigation of this issue, also in other regions. Since heavy snowfall events are rare but contribute strongly to the total precipitation, longer time series are needed. The question of how total precipitation translates into snow accumulation at the surface is complex [*Gorodetskaya et al.*, 2014a, b] and needs to be studied in more detail in the future. The MRR comprises a low-cost, low-maintenance alternative to more complex systems and has been successfully operated at PE during the unmanned winter period. It thus offers potential for investigating snowfall in other polar regions. Special care should be taken to configure the radar with a lower minimum observation height, allowing observations as close to the surface as possible. Also the use of a radar with a higher sensitivity is desirable so that the impact of the blind-zone on events with reflectivities below $-5\,\mathrm{dBz}$ can be investigated. For this, data from the North Slope of Alaska site of the ARM program in Barrow [*Mather and Voyles*, 2012], from the summit station in Greenland [*Shupe et al.*, 2013] or from the Zugspitze in the German alps [*Löhnert et al.*, 2011], as well as possibly from other sites, could be used for future studies.

Acknowledgments.

Part of this work was carried out under the HYDRANT project (http://ees.kuleuven.be/hydrant/) financed by the Belgian Science Policy (EA/01/04AB). MRR data are freely available upon request via the project website (PE) and from the corresponding author M. Maahn (NÅ, LY). CloudSat data were obtained from the CloudSat Data Processing Center (http://www.cloudsat.cira.colostate.edu). The authors would like to thank the International Polar Foundation for logistical support in Antarctica and the staff at the Princess Elisabeth station for supporting this project. We also thank Alexander Mangold (Bel-

gian Royal Meteorological Institute) for help with the instrument maintenance on site. The field work in Svalbard was funded by the European Centre for Arctic Environmental Research (ARCFAC) under research grant number ID2009-146 and by the German Academic Exchange Service (DAAD). The MRR in Ny-Ålesund was courtesy of Clemens Simmer, University of Bonn, and was kindly supervised by the team of the Sverdrup Station of the Norwegian Polar Institut. The MRR in Longyearbyen was courtesy of Chris Kidd, NASA Goddard, and was kindly supervised by Fred Sigernes, Niklas Gantert and Benjamin Merkel (all University Centre in Svalbard). M. Maahn was supported by the project ADMIRARI II of the German Research Association (DFG, LO901/5-1). S. Lhermitte was funded as postdoctoral researcher and K. Van Tricht as aspirant by Fonds Wetenschappelijk Onderzoek - Vlaanderen. The work carried out by S. Kneifel was supported by the German Academic Exchange Service (DAAD) and I. Gorodetskaya was funded by the Belgian Science Policy (EA/01/04AB). The authors would like to thank the three anonymous reviewers for their valuable and constructive comments.

References

Boening, C., M. Lebsock, F. Landerer, and G. Stephens (2012), Snowfall-driven mass change on the East Antarctic ice sheet, *Geophysical Research Letters*, *39*(21), L21,501, doi:10.1029/2012GL053316.

Campbell, J. R., and M. Shiobara (2008), Glaciation of a mixed-phase boundary layer cloud at a coastal arctic site as depicted in continuous lidar measurements, *Polar Science*, *2*(2), 121–127, doi:10.1016/j.polar.2008.04.004.

Clough, S. A., and R. A. A. Franks (1991), The evaporation of frontal and other stratiform precipitation, *Quarterly Journal of the Royal Meteorological Society*, *117*(501), 1057–1080, doi:10.1002/qj.49711750109.

Donovan, D. P., H. W. Barker, R. J. Hogan, T. Wehr, M. Eisinger, D. Lajas, and A. Lefebvre (2013), Scientific aspects of the Earth clouds, aerosols, and radiation explorer (EarthCARE) mission, in *AIP Conference Proceedings*, vol. 1531, pp. 444–447, AIP Publishing, doi:10.1063/1.4804802.

Durden, S., S. Tanelli, and G. Dobrowalski (2011a), CloudSat w-band radar measurements of surface backscatter, *IEEE Geoscience and Remote Sensing Letters*, *8*(3), 401–405, doi:10.1109/LGRS.2010.2079314.

Durden, S. L., S. Tanelli, L. Epp, V. Jamnejad, R. Perez, A. Prata, L. Samoska, E. Long, H. Fang, D. Esteban-Fernandez, and others (2011b), A cloud and precipitation radar system concept for the ACE mission, Jet Propulsion Laboratory, National Aeronautics and Space Administration, Pasadena, CA, Vancouver, Canada.

Evans, E., R. E. Stewart, W. Henson, and K. Saunders (2011), On precipitation and virga over three locations during the 19992004 Canadian prairie drought, *Atmosphere-Ocean*, *49*(4), 366–379, doi:10.1080/07055900.2011.608343.

Fabry, F., and I. Zawadzki (1995), Long-term radar observations of the melting layer of precipitation and their interpretation, *Journal of the Atmospheric Sciences*, *52*(7), 838–851, doi:10.1175/1520-0469(1995)052¡0838:LTROOT¿2.0.CO;2.

Førland, E. J., R. Benestad, I. Hanssen-Bauer, J. E. Haugen, and T. E. Skaugen (2012), Temperature and precipitation development at Svalbard 1900-2100, *Advances in Meteorology*, *2011*, doi:10.1155/2011/893790.

Gammelsrød, T., and B. Rudels (1983), Hydrographic and current measurements in the Fram Strait, August 1981, *Polar Research*, *1*(2), 115–126, doi:10.1111/j.1751-8369.1983.tb00696.x.

Gelsthorpe, R. V., A. Heliere, A. Lefebvre, J. Lemanczyk, E. Mateu, A. Perez-Albinana, and K. Wallace (2010), Aspects of the EarthCARE satellite and its payload, in *Proc. SPIE 7826, Sensors, Systems, and Next-Generation Satellites XIV, 78260G (October 13, 2010)*, vol. 7826, pp. 78,260G–78,260G–11, doi:10.1117/12.868382.

Gorodetskaya, I. V., N. P. M. Van Lipzig, M. R. Van den Broeke, A. Mangold, W. Boot, and C. H. Reijmer (2013), Meteorological regimes and accumulation patterns at Utsteinen, Dronning Maud land, East Antarctica: Analysis of two contrasting years, *Journal of Geophysical Research: Atmospheres*, *118*(4), 1700–1715, doi:10.1002/jgrd.50177.

Gorodetskaya, I. V., S. Kneifel, M. Maahn, K. Van Tricht, J. H. Schween, S. Crewell, and N. P. M. Van Lipzig (2014a), Cloud and precipitation properties from ground-based remote sensing instruments in east antarctica, *The Cryosphere Discussions*, *8*(4), 4195–4241, doi:10.5194/tcd-8-4195-2014.

Gorodetskaya, I. V., M. Tsukernik, K. Claes, M. F. Ralph, W. D. Neff, and N. P. M. Van Lipzig (2014b), The role of atmospheric rivers in anomalous snow accumulation in east antarctica, *Geophysical Research Letters*, *41*(17), 6199–6206, doi:10.1002/2014GL060881.

Henson, W., R. Stewart, and D. Hudak (2011), Vertical reflectivity profiles of precipitation over Iqaluit, Nunavut during autumn 2007, *Atmospheric Research*, *99*, 217–229, doi:10.1016/j.atmosres.2010.10.009.

Hiley, M. J., M. S. Kulie, and R. Bennartz (2011), Uncertainty analysis for CloudSat snowfall retrievals, *Journal of Applied Meteorology and Climatology*, *50*(2), 399–418, doi:10.1175/2010JAMC2505.1.

Hou, A. Y., R. K. Kakar, S. Neeck, A. A. Azarbarzin, C. D. Kummerow, M. Kojima, R. Oki, K. Nakamura, and T. Iguchi (2014), The global precipitation measurement mission, *Bulletin of the American Meteorological Society*, *95*(5), 701–722, doi:10.1175/BAMS-D-13-00164.1.

Joe, P., C. Kidd, P. Kollias, S. Tanelli, D. Moisseev, A. Battaglia, J. Koikinen, G. Arbery, B. Deligny, E. Caubet, and others (2010), The polar precipitation measurement mission, in *Proc. 6th European Conference on Radar Meteorology and Hydrology: Satellite radar measurements and hydro-met eorological applications, Sibiu, Romania*, p. 610.

Klugmann, D., K. Heinsohn, and H.-J. Kirtzel (1996), A low cost 24 GHz FM-CW Doppler radar rain profiler, *Contributions to Atmospheric Physics*, *69*(1), 247–253.

Kneifel, S., M. Maahn, G. Peters, and C. Simmer (2011), Observation of snowfall with a low-power FM-CW K-band radar (Micro Rain Radar), *Meteorology and Atmospheric Physics*, *113*(1-2), 75–87, doi:10.1007/s00703-011-0142-z.

Kneifel, S., S. Redl, E. Orlandi, U. Löhnert, M. P. Cadeddu, D. D. Turner, and M.-T. Chen (2014), Absorption properties of supercooled liquid water between 31 and 225 GHz: evaluation of absorption models using ground-based observations, *Journal of Applied Meteorology and Climatology*, *53*(4), 1028–1045, doi:10.1175/JAMC-D-13-0214.1.

Knuth, S. L., G. J. Tripoli, J. E. Thom, and G. A. Weidner (2010), The influence of blowing snow and precipitation on snow depth change across the Ross ice shelf and Ross sea regions of Antarctica, *Journal of Applied Meteorology and Climatology*, *49*(6),

1306–1321, doi:10.1175/2010JAMC2245.1.

Kulie, M. S., and R. Bennartz (2009), Utilizing spaceborne radars to retrieve dry snowfall, *Journal of Applied Meteorology and Climatology*, *48*(12), 2564–2580, doi: 10.1175/2009JAMC2193.1.

Lenaerts, J. T. M., M. R. van den Broeke, W. J. van de Berg, E. van Meijgaard, and P. Kuipers Munneke (2012), A new, high-resolution surface mass balance map of Antarctica (19792010) based on regional atmospheric climate modeling, *Geophysical Research Letters*, *39*(4), L04,501, doi:10.1029/2011GL050713.

Levizzani, V., S. Laviola, and E. Cattani (2011), Detection and measurement of snowfall from space, *Remote Sensing*, *3*(1), 145–166, doi:10.3390/rs3010145.

Liu, G. (2008a), Deriving snow cloud characteristics from CloudSat observations, *Journal of Geophysical Research*, *113*(D8), D00A09, doi:10.1029/2007JD009766.

Liu, G. (2008b), A database of microwave single-scattering properties for nonspherical ice particles, *Bulletin of the American Meteorological Society*, *89*(10), 1563–1570, doi: 10.1175/2008BAMS2486.1.

Löffler-Mang, M., and J. Joss (2000), An optical disdrometer for measuring size and velocity of hydrometeors, *Journal of Atmospheric and Oceanic Technology*, *17*(2), 130–139, doi:10.1175/1520-0426(2000)017¡0130:AODFMS¿2.0.CO;2.

Löhnert, U., S. Kneifel, A. Battaglia, M. Hagen, L. Hirsch, and S. Crewell (2011), A multisensor approach toward a better understanding of snowfall microphysics: The TOSCA project, *Bulletin of the American Meteorological Society*, *92*(5), 613-628, doi: 10.1175/2010BAMS2909.1.

L'Ecuyer, T. S., and J. H. Jiang (2010), Touring the atmosphere aboard the A-Train, *Physics Today*, *63*(7), 36–41, doi:10.1063/1.3463626.

Maahn, M., and P. Kollias (2012), Improved Micro Rain Radar snow measurements using doppler spectra post-processing, *Atmos. Meas. Tech.*, *5*(11), 2661–2673, doi:10.5194/amt-5-2661-2012.

Mace, G. G. (2006), Level 2 GEOPROF product process description and interface control document. Available at http://www.cloudsat.cira.colostate.edu/ICD/2B-GEOPROF/2B-GEOPROF_PDICD_5.3.doc (Accessed 23 Mai 2014).

Marchand, R., G. G. Mace, T. Ackerman, and G. Stephens (2008), Hydrometeor detection using *Cloudsat* An Earth-orbiting 94-GHz cloud radar, *Journal of Atmospheric and Oceanic Technology*, *25*(4), 519–533, doi:10.1175/2007JTECHA1006.1.

Mather, J. H., and J. W. Voyles (2012), The arm climate research facility: A review of structure and capabilities, *Bulletin of the American Meteorological Society*, *94*(3), 377–392, doi:10.1175/BAMS-D-11-00218.1.

Matrosov, S. Y. (2007), Modeling backscatter properties of snowfall at millimeter wavelengths, *Journal of the Atmospheric Sciences*, *64*(5), 1727–1736, doi:10.1175/JAS3904.1.

Matrosov, S. Y., and A. Battaglia (2009), Influence of multiple scattering on CloudSat measurements in snow: A model study, *Geophys. Res. Lett.*, *36*(12), L12,806, doi:10.1029/2009GL038704.

Noone, D., J. Turner, and R. Mulvaney (1999), Atmospheric signals and characteristics of accumulation in Dronning Maud Land, Antarctica, *Journal of Geophysical Research: Atmospheres*, *104*(D16), 19,191–19,211, doi:10.1029/1999JD900376.

Palerme, C., J. E. Kay, C. Genthon, T. L'Ecuyer, N. B. Wood, and C. Claud (2014), How much snow falls on the Antarctic ice sheet?, *The Cryosphere Discuss.*, *8*(1), 1279–1304, doi:10.5194/tcd-8-1279-2014.

Peters, G., B. Fischer, and T. Andersson (2002), Rain observations with a vertically looking Micro Rain Radar (MRR), *Boreal Environment Research*, *7*(4), 353362.

Peters, G., B. Fischer, H. Münster, M. Clemens, and A. Wagner (2005), Profiles of raindrop size distributions as retrieved by Microrain Radars, *Journal of Applied Meteorology*, *44*(12), 1930–1949, doi:10.1175/JAM2316.1.

Protat, A., D. Bouniol, J. Delano, E. O'Connor, P. T. May, A. Plana-Fattori, A. Hasson, U. Görsdorf, and A. J. Heymsfield (2009), Assessment of Cloudsat reflectivity measurements and ice cloud properties using ground-based and airborne cloud radar observations, *Journal of Atmospheric and Oceanic Technology*, *26*(9), 1717–1741, doi:10.1175/2009JTECHA1246.1.

Protat, A., J. Delano, E. J. O'Connor, and T. S. L'Ecuyer (2010), The evaluation of CloudSat and CALIPSO ice microphysical products using ground-based cloud radar and lidar observations, *Journal of Atmospheric and Oceanic Technology*, *27*(5), 793–810, doi:10.1175/2009JTECHA1397.1.

Schlosser, E., K. W. Manning, J. G. Powers, M. G. Duda, G. Birnbaum, and K. Fujita (2010), Characteristics of high-precipitation events in Dronning Maud Land, Antarctica, *Journal of Geophysical Research: Atmospheres*, *115*(D14), D14,107, doi:10.1029/2009JD013410.

Schneider, U., A. Becker, P. Finger, A. Meyer-Christoffer, M. Ziese, and B. Rudolf (2014), GPCC's new land surface precipitation climatology based on quality-controlled in situ

data and its role in quantifying the global water cycle, *Theoretical and Applied Climatology*, *115*(1-2), 15–40, doi:10.1007/s00704-013-0860-x.

Serreze, M. C., F. Carse, R. G. Barry, and J. C. Rogers (1997), Icelandic low cyclone activity: Climatological features, linkages with the NAO, and relationships with recent changes in the northern hemisphere circulation, *Journal of Climate*, *10*(3), 453–464, doi:10.1175/1520-0442(1997)010¡0453:ILCACF¿2.0.CO;2.

Shupe, M. D., D. D. Turner, V. P. Walden, R. Bennartz, M. P. Cadeddu, B. B. Castellani, C. J. Cox, D. R. Hudak, M. S. Kulie, N. B. Miller, R. R. Neely, W. D. Neff, and P. M. Rowe (2013), High and dry: New observations of tropospheric and cloud properties above the greenland ice sheet, *Bulletin of the American Meteorological Society*, *94*(2), 169–186, doi:10.1175/BAMS-D-11-00249.1.

Smalley, M., T. L'Ecuyer, M. Lebsock, and J. Haynes (2014), A comparison of precipitation occurrence from the NCEP stage IV QPE product and the CloudSat cloud profiling radar, *Journal of Hydrometeorology*, *15*(1), 444–458, doi:10.1175/JHM-D-13-048.1.

Stark, D., B. A. Colle, and S. E. Yuter (2013), Observed microphysical evolution for two East Coast winter storms and the associated snow bands, *Monthly Weather Review*, *141*(6), 2037–2057, doi:10.1175/MWR-D-12-00276.1.

Stephens, G. L., D. G. Vane, S. Tanelli, E. Im, S. Durden, M. Rokey, D. Reinke, P. Partain, G. G. Mace, R. Austin, T. L'Ecuyer, J. Haynes, M. Lebsock, K. Suzuki, D. Waliser, D. Wu, J. Kay, A. Gettelman, Z. Wang, and R. Marchand (2008), CloudSat mission: Performance and early science after the first year of operation, *Journal of Geophysical Research*, *113*, D00A18, doi:10.1029/2008JD009982.

Stewart, R. E., J. E. Burford, D. R. Hudak, B. Currie, B. Kochtubajda, P. Rodriguez, and J. Liu (2004), Weather systems occurring over Fort Simpson, Northwest Territories, Canada, during three seasons of 19981999: 2. precipitation features, *Journal of Geophysical Research: Atmospheres*, *109*(D22), D22,109, doi:10.1029/2004JD004929.

Tanelli, S., S. Durden, E. Im, K. Pak, D. Reinke, P. Partain, J. Haynes, and R. Marchand (2008), CloudSat's cloud profiling radar after two years in orbit: Performance, calibration, and processing, *IEEE Transactions on Geoscience and Remote Sensing*, *46*(11), 3560–3573, doi:10.1109/TGRS.2008.2002030.

Thode, H. C. (2002), *Testing For Normality*, Marcel Dekker, New York.

Tridon, F., J. V. Baelen, and Y. Pointin (2011), Aliasing in micro rain radar data due to strong vertical winds, *Geophysical Research Letters*, *38*, L02,804, doi:10.1029/2010GL046018.

Tsukernik, M., D. N. Kindig, and M. C. Serreze (2007), Characteristics of winter cyclone activity in the northern North Atlantic: Insights from observations and regional modeling, *Journal of Geophysical Research: Atmospheres*, *112*(D3), D03,101, doi:10.1029/2006JD007184.

Wang, Z., K. Sassen, D. N. Whiteman, and B. B. Demoz (2004), Studying altocumulus with ice virga using ground-based active and passive remote sensors, *Journal of Applied Meteorology*, *43*(3), 449–460, doi:10.1175/1520-0450(2004)043¡0449:SAWIVU¿2.0.CO;2.

Wolfe, J. P., and J. R. Snider (2012), A relationship between reflectivity and snow rate for a high-altitude S-Band radar, *Journal of Applied Meteorology and Climatology*, *51*(6), 1111–1128, doi:10.1175/JAMC-D-11-0112.1.

Wood, N. B. (2011), Estimation of snow microphysical properties with application to millimeter-wavelength radar retrievals for snowfall rate, Ph.D. thesis, Colorado State University. Available at http://digitool.library.colostate.edu/R/?func=dbin-jump-full&object_id=123397 (Accessed 23 Mai 2014).

Wood, N. B., T. S. L'Ecuyer, D. G. Vane, G. L. Stephens, and P. Partain (2013), Level 2C snow profile process description and interface control document. Available at *http://www.cloudsat.cira.colostate.edu/ICD/2C-SNOW-PROFILE/2C-SNOW-PROFILE_PDICD_P_R04.pdf* (Accessed 23 Mai 2014).

Xiao, J., R. Bintanja, S. J. Dry, G. W. Mann, and P. A. Taylor (2000), An intercomparison among four models of blowing snow, *Boundary-Layer Meteorology*, *97*(1), 109–135, doi: 10.1023/A:1002795531073.

Yang, D., E. Elomaa, A. Tuominen, A. Aaltonen, B. Goodison, T. Gunther, V. Golubev, B. Sevruk, H. Madsen, and J. Milkovic (1999), Wind-induced precipitation undercatch of the Hellmann gauges, *Nordic hydrology*, *30*(1), 57–80.

Table 1. Comparison of MRR and CloudSat's CPR.

	MRR	CPR
Frequency (GHz)	24.23	94.05
Radar type	FMCW	Pulsed
Transmit power (W)	0.05	1820 (peak power)
Radar Power consumption (W)	25	–
No. of range gates	31	125
Range resolution (m)	100/60[a]	485, resampled to 240
Measuring range (km)	0-3/0-1.8[a]	0-25
Lowest usable range gate (m)	400/240[a]	1200
Antenna diameter (m)	0.6	1.85
Beam width (2-way, 6 dB)	1.5 °	0.12 °
Minimum Detectable Z (dBz)	-5 at 1200 m agl	-30
Integration Time (s)	300	0.16
Cross-track Resolution (km)	–	1.4
Along-track Resolution (km)	–	1.8

[a] depending on configuration

Table 2. Equivalent reflectivity − snowfall rate ($Z_e - S$) relations from *Kulie and Bennartz* [2009] and derived conversion for Z_e from 35 GHz to 94 GHz.

particle habit	Z_e (35 GHz)	Z_e (94 GHz)	Z_e conv. from 35 to 94 GHz
Three bullet rosette (LR3)	$24.04S^{1.51}$	$13.16S^{1.40}$	$0.69Z_e^{0.93}$
Aggregates (HA)	$313.29S^{1.85}$	$56.43S^{1.52}$	$0.50Z_e^{0.82}$
Snow (SS)	$19.66S^{1.74}$	$2.19S^{1.20}$	$0.28Z_e^{0.69}$

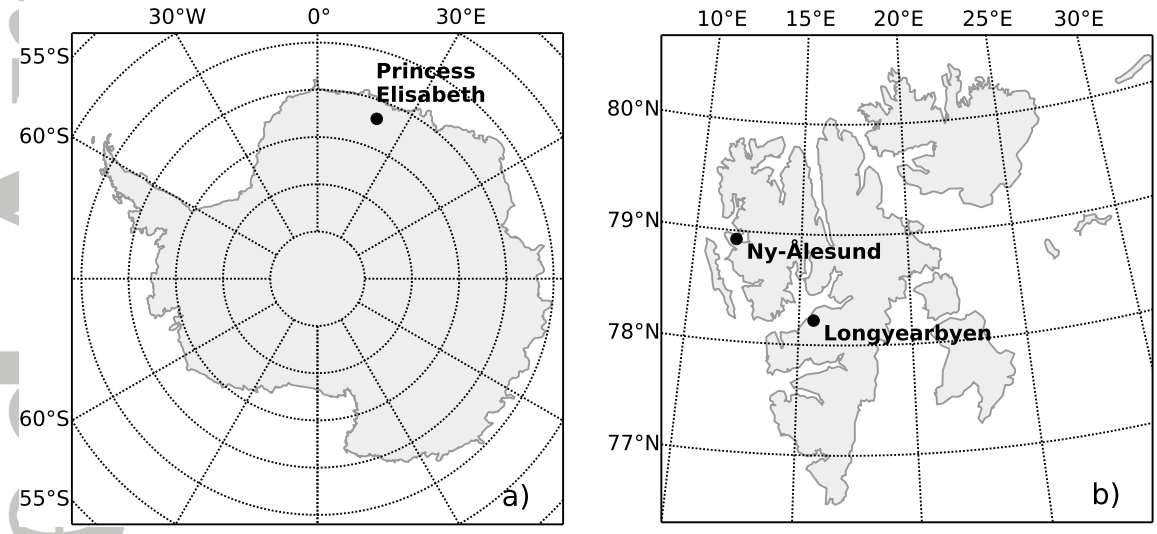

Figure 1. Map of the location of Princess Elisabeth Station in East Antarctica (a) and of Ny-Ålesund and Longyearbyen in Svalbard, Norway (b).

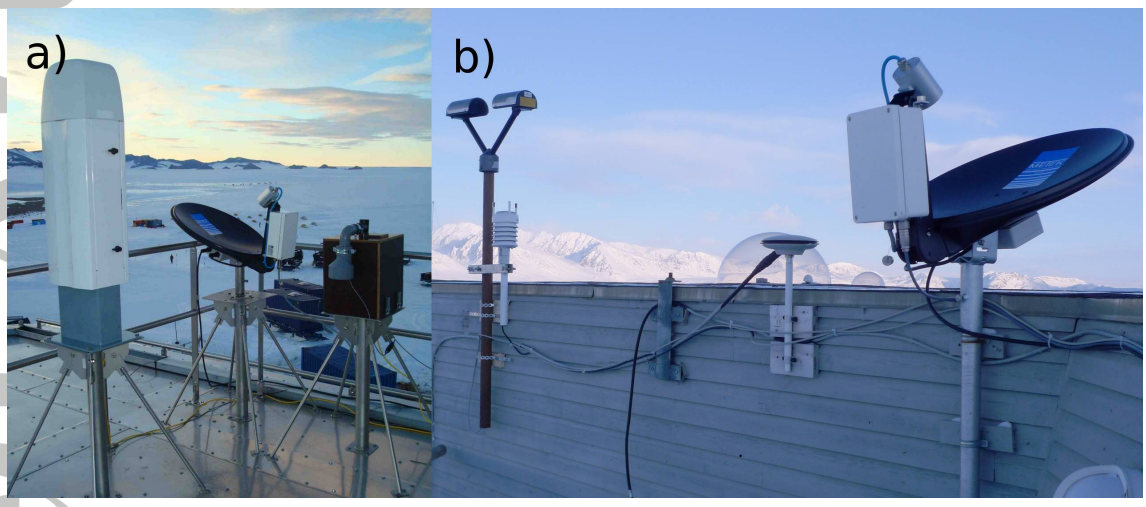

Figure 2. a) Ceilometer (left), MRR (middle), and infrared Pyrometer (right) on the roof of the Belgian Princess Elisabeth Station in East Antarctica. b) MRR (right) and Parsivel disdrometer on the roof of the Norwegian Polar Institute Sverdrup Station in Ny-Ålesund, Svalbard.

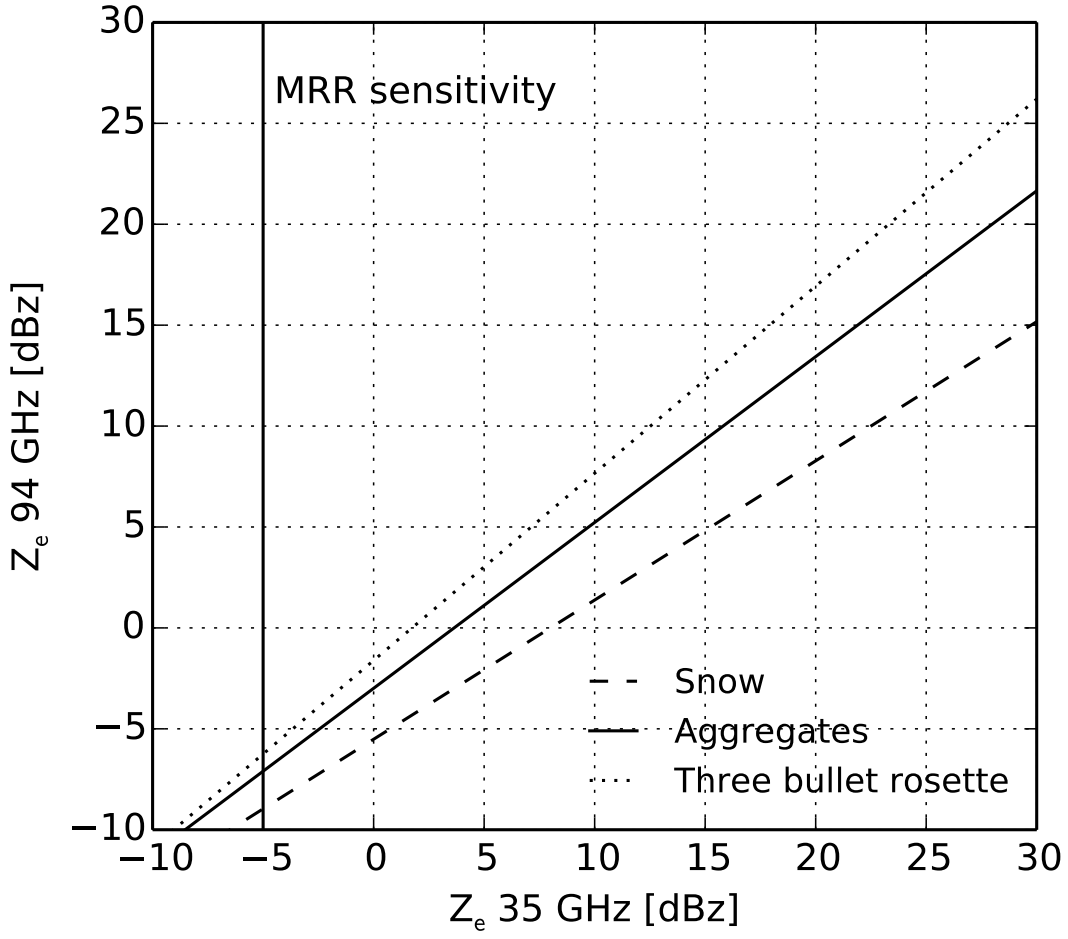

Figure 3. Conversion of reflectivity Z_e from 35 GHz to 94 GHz for snow (dashed), aggregates (solid) and three bullet rosettes (dotted) derived from the $Z_e - S$ relations of *Kulie and Bennartz* [2009].

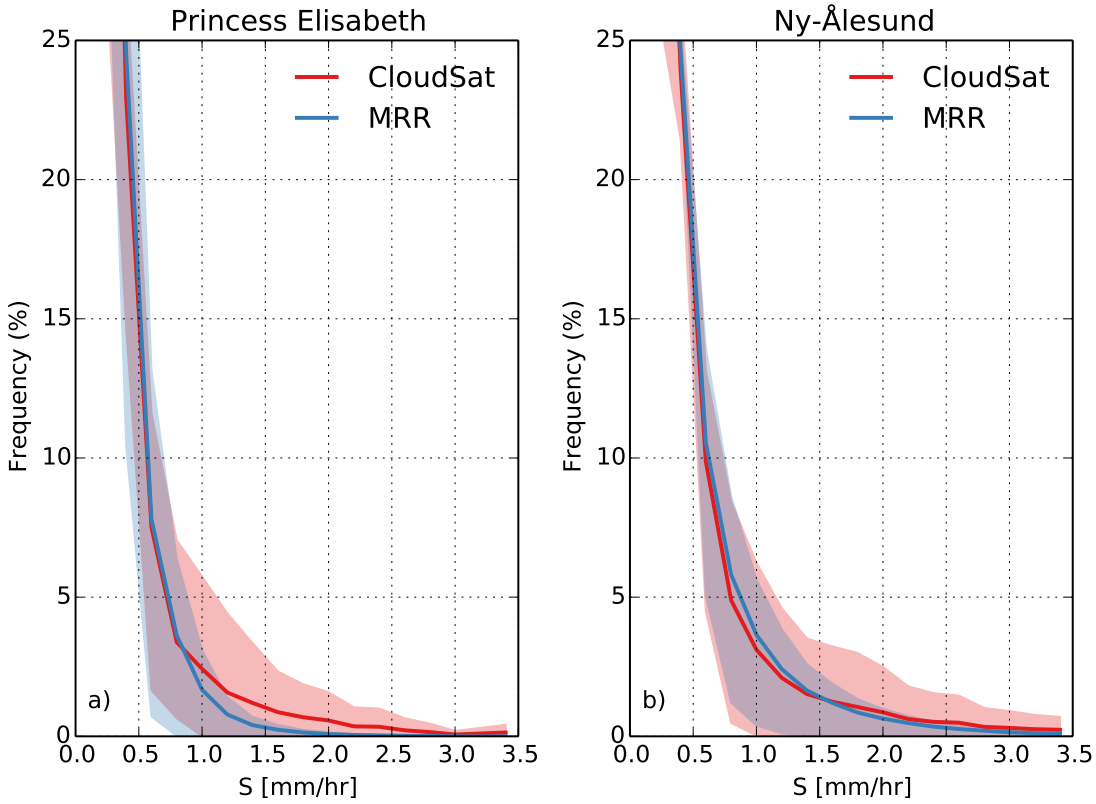

Figure 4. Frequency distribution of snowfall rates S for CloudSat (red) and MRR (blue) data at 1200 m agl (H_{CS}) for the Princess Elisabeth (a) and Ny-Ålesund (b) stations, where snowfall rate was determined by the range of $Z_e - S$ relationships in *Kulie and Bennartz* [2009]. The line/polygon represents the mean/range of S for these $Z_e - S$ relationships.

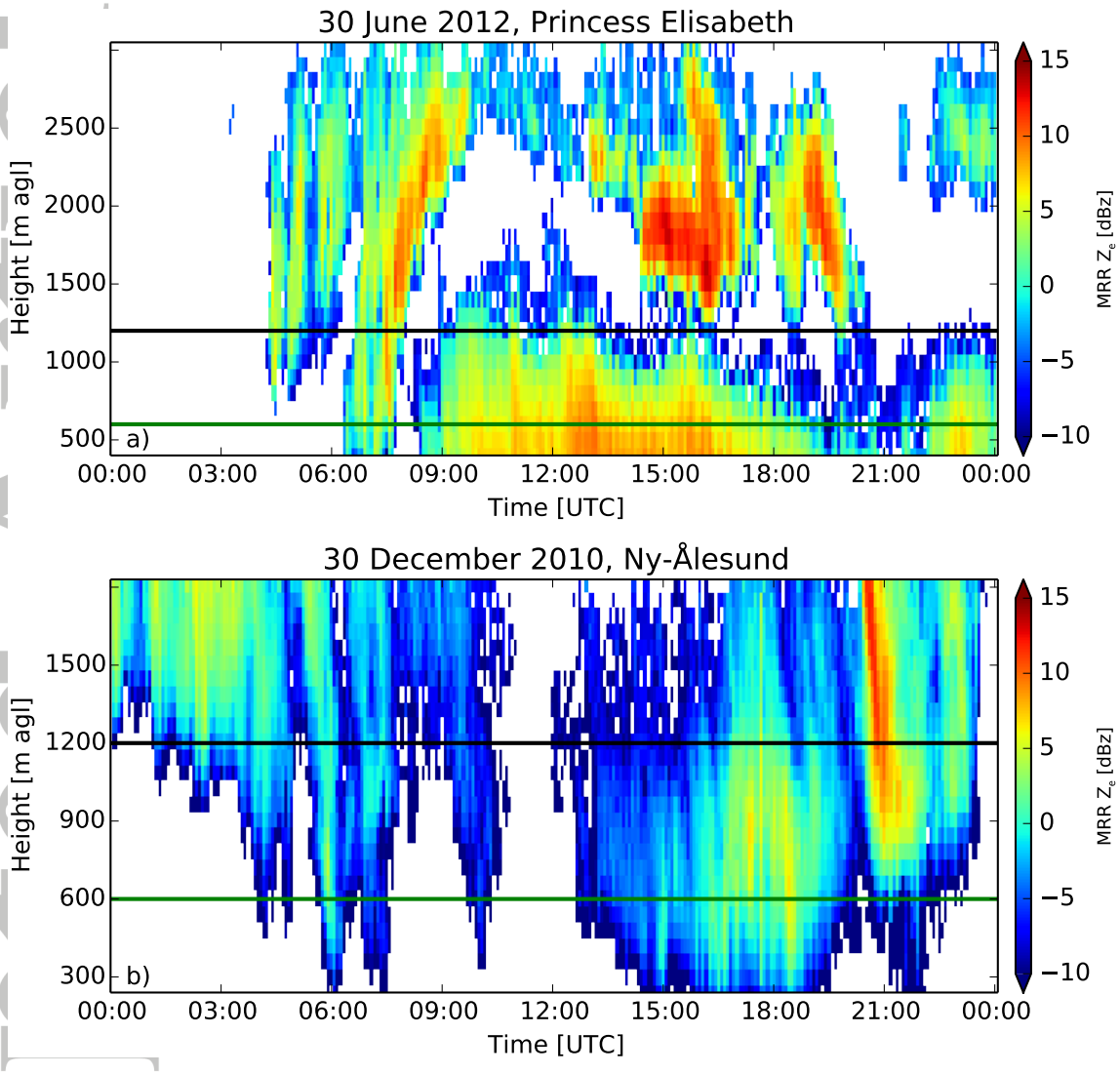

Figure 5. Time-height plots of reflectivity Z_e for two cases at Princess Elisabeth (a) and Ny-Ålesund (b). CloudSat's blind-zone of 1200 m agl (H_{CS}) and a reduced blind-zone of 600 m agl (H_{FM}) are denoted by a black and green line, respectively.

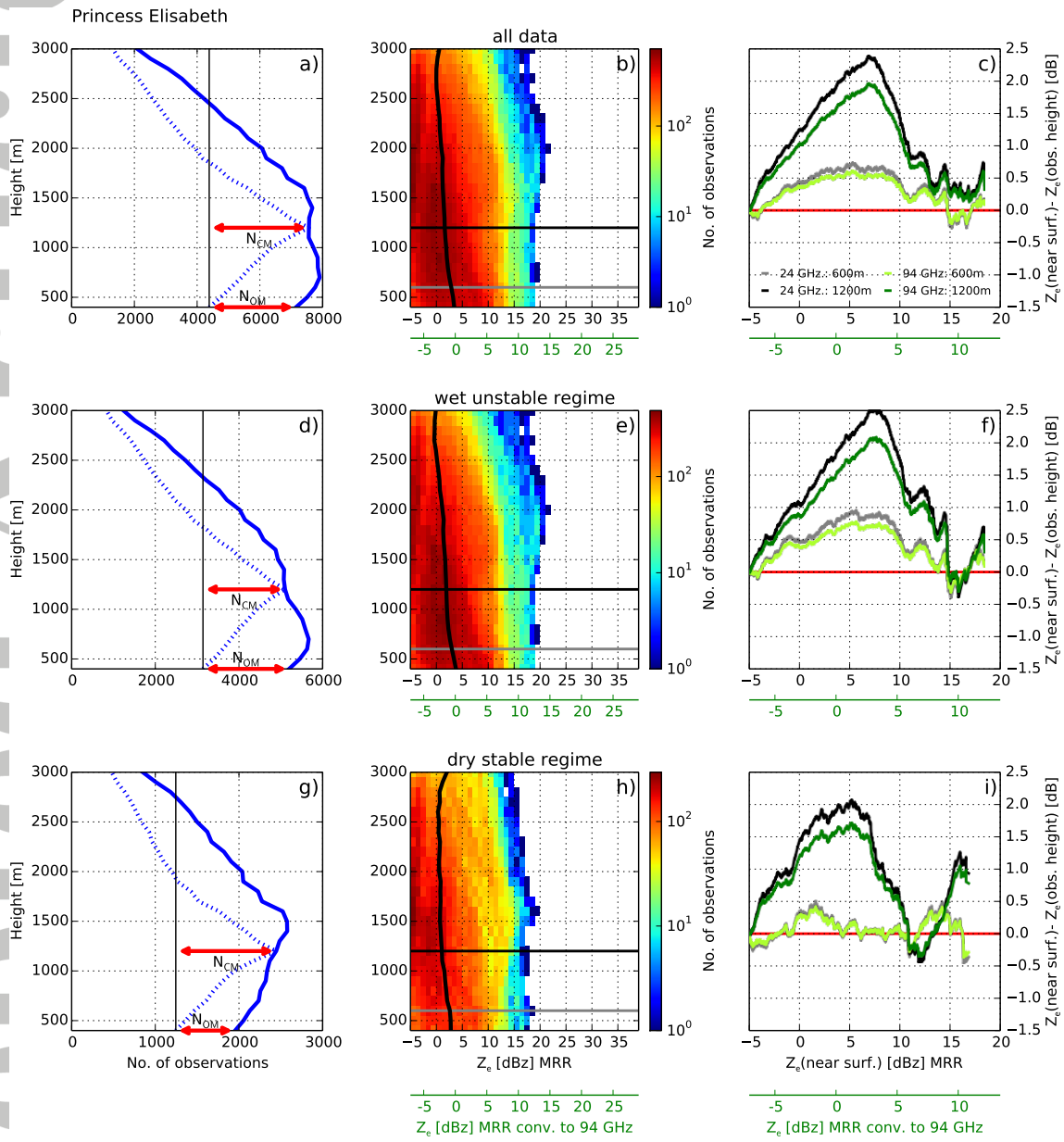

Figure 6. see next page for caption.

Figure 6. Left Column: total number of observations N with Z_e of MRR observations at Princess Elisabeth Station, East Antarctica larger than $-5\,\mathrm{dBz}$ (solid blue line) are compared with profiles $\hat{N}$, which also contain snowfall at 1200 m agl (dashed blue line). The comparison is presented for the complete dataset (top row), the *dry stable regime* (center row) and the *wet unstable regime* (bottom row). Commission and omission error (N_{CM} and N_{OM}) are marked with red arrows. Center column: reflectivity vs. altitude 2D histograms (2DH) of observed MRR reflectivities. The median profile is denoted by the black solid line. The horizontal, black line denotes H_{CS}. A reduced blind-zone of 600 m agl (H_{FM}) of a future satellite mission is marked with a horizontal, gray line. An estimate for the corresponding Z_e at 94 GHz using the coefficients for aggregates is indicated by the additional, green scale. Right column: Detrended Quantile-Quantile (DQQ) plots of the reflectivity observations close to the surface (H_{SF}) in comparison to H_{CS} (black) and in comparison to H_{FM} (gray) as well as after conversion to 94 GHz (green and light-green lines). In contrast to a Quantile-Quantile plot, only the differences between quantiles of Z_e at H_{CS} (or H_{FM}) and H_{SF} are shown for the ordinate, i. e., a value of zero means perfect agreement.

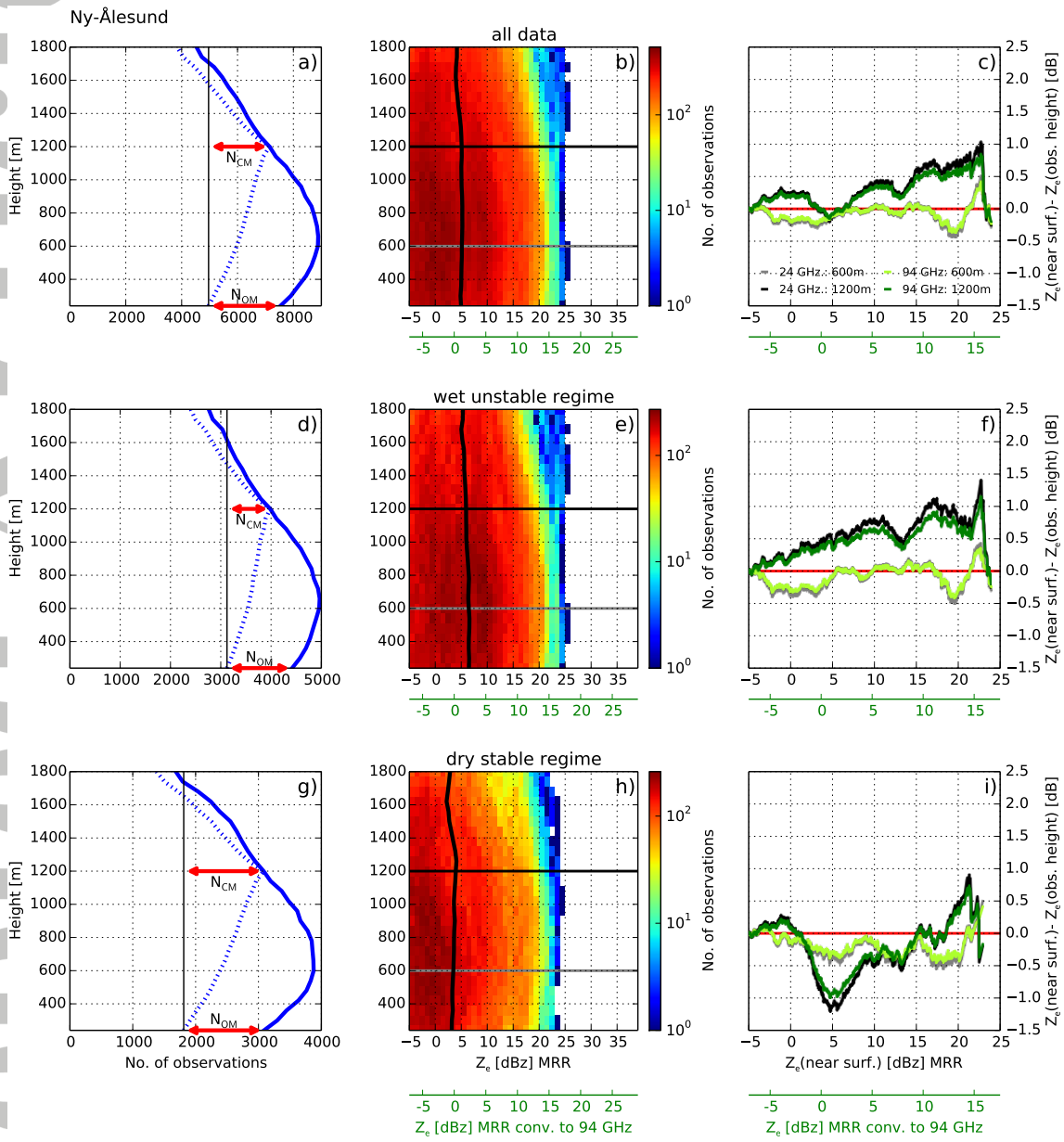

Figure 7. Same as Fig. 6, but for Ny-Ålesund, Svalbard.

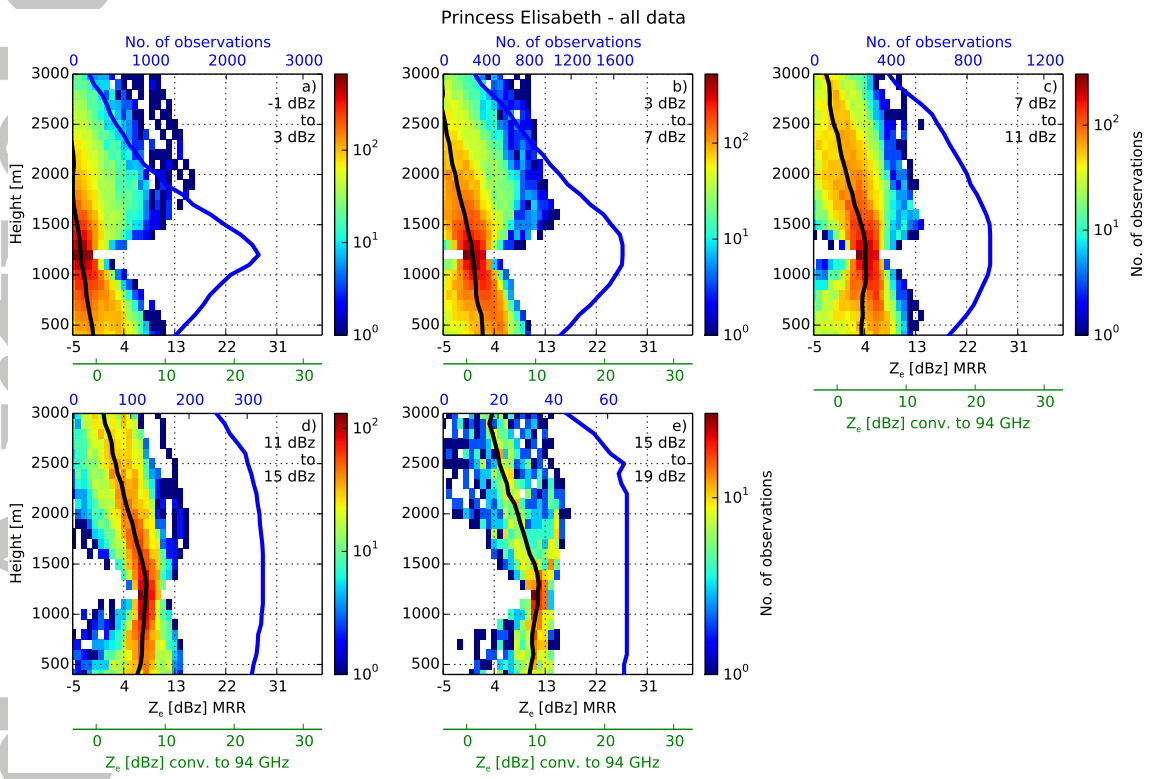

Figure 8. Reflectivity vs. altitude 2D histogram (2DH) of MRR observations at Princess Elisabeth Station, East Antarctica. The presented dataset is limited to profiles which are within a certain reflectivity threshold at the CloudSat reference height of 1200 m agl (H_{CS}): While (a) shows only profiles that are between −1 and 3 dBz at the reference height, the other ones are limited to reflectivities of −5, 9, 13 and 17±2 dBz, respectively. The median is denoted in black, the total number of observation greater −5 dBz per height in blue. An estimate for the corresponding Z_e at 94 GHz using the coefficients for aggregates is indicated by the additional, green scale.

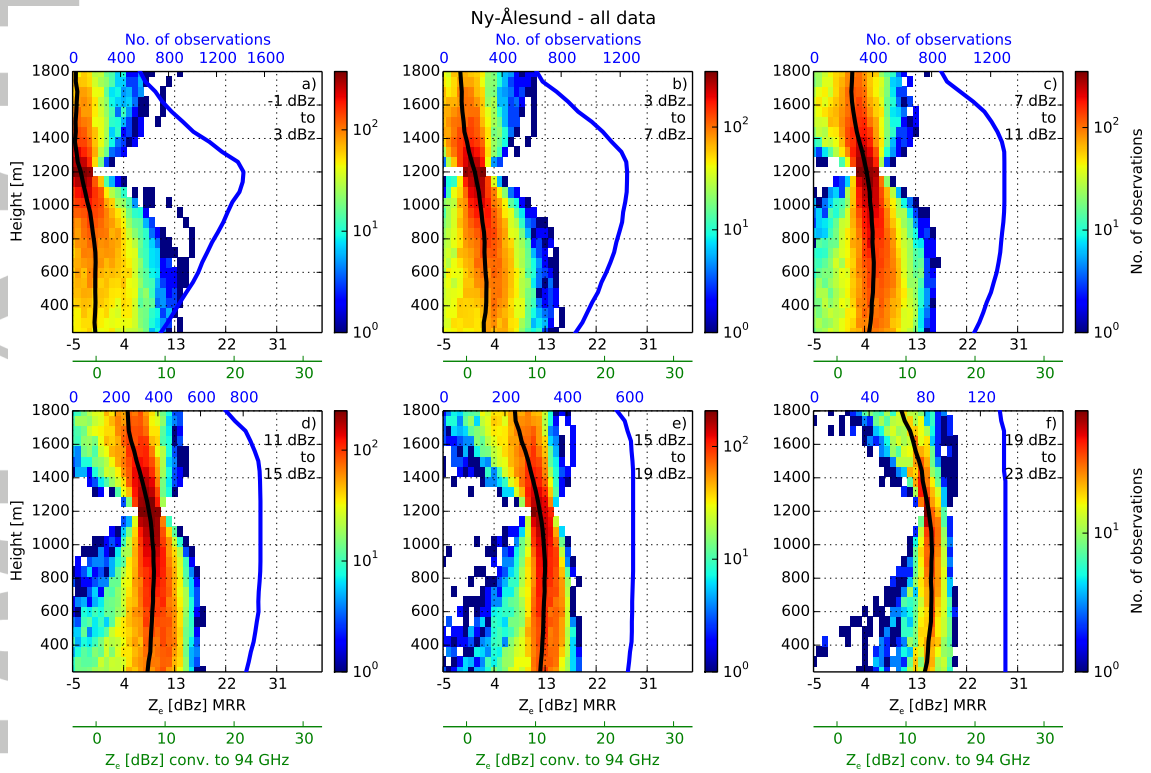

Figure 9. Same as Fig. 8, but for Ny-Ålesund with an additional panel (f) for the 19 to 23 dBz interval.

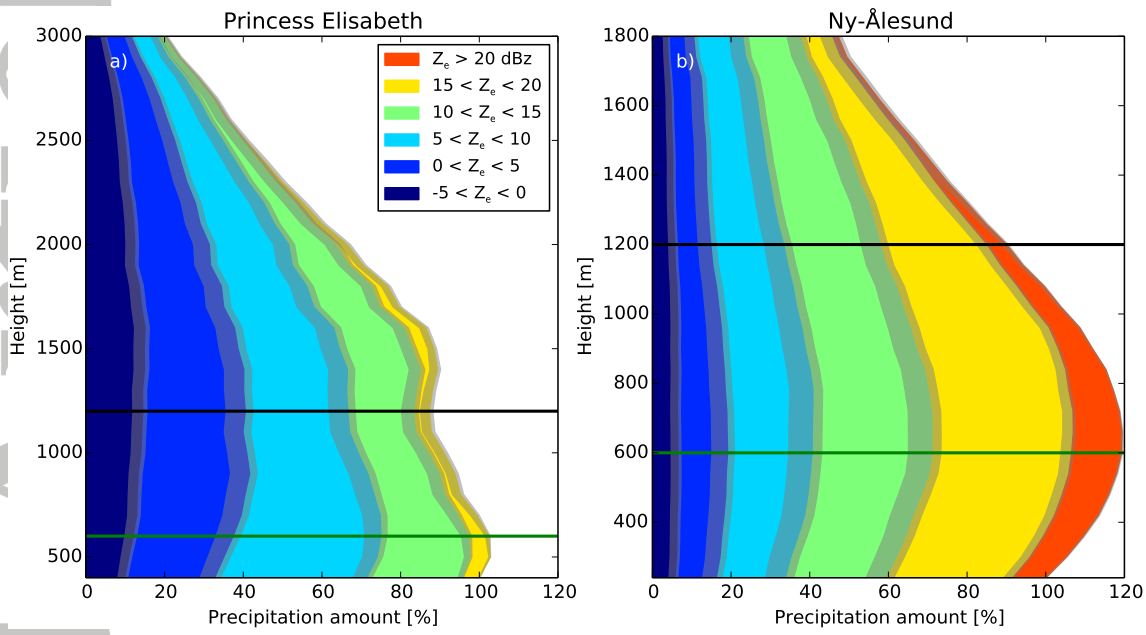

Figure 10. Contribution of various reflectivity intervals to the total precipitation amount in dependence on height for Princess Elisabeth and Ny-Ålesund. For the colored areas, the $Z_e - S$ relation by *Kulie and Bennartz* [2009] for *snow* is used. Uncertainty of the borders between the different intervals due to the $Z_e - S$ relations is estimated by the gray, shaded area, which is estimated by applying also $Z_e - S$ relations for *three bullet rosettes* and *aggregates* by *Kulie and Bennartz* [2009]. The figures are normalized by total surface precipitation. CloudSat's blind-zone of 1200 m agl (H_{CS}) and a reduced blind-zone of 600 m agl (H_{FM}) are denoted by black and green lines, respectively.